

Hydrodynamical constraints on the bubble wall velocityTomasz Krajewski^{1,*}, Marek Lewicki^{2,†} and Mateusz Zych^{2,‡}¹*Nicolaus Copernicus Astronomical Center, ul. Bartycka 18, 00-716 Warsaw, Poland*²*Faculty of Physics, University of Warsaw, ul. Pasteura 5, 02-093 Warsaw, Poland* (Received 14 April 2023; revised 26 June 2023; accepted 11 September 2023; published 17 November 2023)

Terminal velocity reached by bubble walls in first-order phase transitions is an important parameter determining both primordial gravitational wave spectrum and the production of baryon asymmetry in models of electroweak baryogenesis. We developed a numerical code to study the real-time evolution of expanding bubbles and investigate how their walls reach stationary states. Our results agree with profiles obtained within the so-called bag model with very good accuracy; however, not all such solutions are stable and realized in dynamical systems. Depending on the exact shape of the potential there is always a range of wall velocities where no steady-state solutions exist. This behavior in deflagrations was explained by hydrodynamical obstruction where solutions that would heat the plasma outside the wall above the critical temperature and cause local symmetry restoration are forbidden. For even more affected hybrid solutions causes are less straightforward. However, we provide a simple numerical fit allowing one to verify if a solution with a given velocity is allowed simply by computing the ratio of the nucleation temperature to the critical one for the potential in question.

DOI: [10.1103/PhysRevD.108.103523](https://doi.org/10.1103/PhysRevD.108.103523)**I. INTRODUCTION**

Phase transitions are a common feature of particle physics models. If they are first order they can open a path to numerous phenomena such as the production of both the baryon asymmetry [1–4] and a stochastic background of gravitational waves (GWs) [5–8]. Significant progress has been made recently in understanding fine details of the dynamics of such transitions necessary to describe the intricate relation between these possibilities [9–17]. Despite that, determining the bubble wall velocity in the stationary state remains a problem. Given its impact on both the amplitude of the GW signal as well as the production of the baryon asymmetry, this issue needs to be solved in order to finally pinpoint the interplay between these two signals.

Contrary to nucleation temperature or transition strength, the wall velocity is not a straightforward consequence of the shape of the effective potential. The standard Wentzel-Kramers-Brillouin (WKB) method of computing the velocity involves solving a set of Boltzmann equations in the vicinity of the bubble wall in order to find the friction the plasma will enact on the expanding wall. However, the result still crucially relies on the hydrodynamical solution for the plasma profile [13,15,18]. It is a standard practice to use the plasma behavior obtained in the bag model in

these studies. The obvious drawback of this approach is that the bag equation of state (EOS) inherently neglects all knowledge of the potential except the energy difference between its minima [19].

In this work, we investigate the impact that features of the potential have on hydrodynamical solutions for the plasma. To this end, we perform lattice simulations tracking the real-time evolution of the scalar profiles coupled to the plasma that describe a single expanding bubble. We use novel methods that allow us to properly resolve shocks forming in the fluid and prevent the appearance of unphysical artifacts. This allows us to study for the first time in detail the evolution of the system for relatively strong transitions and fastest walls that still form heated fluid shells around bubbles. Increased temperature results in large baryon yields while large transition strength and wall velocity provide a strong GW signal making this part of the parameter space the most promising for the realization of both [9,14,15,17]. We find that the problem of hydrodynamical obstruction [20] persists for stronger transitions and faster walls rendering a large class of solutions unstable. This constitutes a forbidden range for bubble wall velocities particularly impacting the most promising solutions with the fastest walls which still lead to a formation of heated fluid shells surrounding the bubbles.

II. THE MODEL: SCALAR FIELD COUPLED TO PERFECT FLUID

In this work, we investigate a system consisting of the scalar field ϕ coupled to the perfect fluid described by its

*tkrajewski@camk.edu.pl

†marek.lewicki@fuw.edu.pl

‡mateusz.zych@fuw.edu.pl

temperature T and local flow four-velocity u [21–25]. The equation of state is given by

$$\epsilon(\phi, T) = 3aT^4 + V(\phi, T) - T \frac{\partial V}{\partial T}, \quad (1)$$

$$p(\phi, T) = aT^4 - V(\phi, T), \quad (2)$$

where $a = (\pi^2/90)g_*$ and $w \equiv \epsilon + p$. For the effective potential $V(\phi, T)$ we use a simple polynomial potential augmented with high-temperature corrections parametrized as

$$V(\phi, T) = \frac{1}{2}\gamma(T^2 - T_0^2)\phi^2 - \frac{1}{3}\delta T\phi^3 + \frac{1}{4}\lambda\phi^4. \quad (3)$$

The energy-momentum tensor of the system is a sum of energy-momentum tensors for the field and the fluid,

$$T_{\text{field}}^{\mu\nu} = \partial^\mu\phi\partial^\nu\phi - g^{\mu\nu}\left(\frac{1}{2}\partial_\alpha\phi\partial^\alpha\phi\right), \quad (4)$$

$$T_{\text{fluid}}^{\mu\nu} = wu^\mu u^\nu + g^{\mu\nu}p, \quad (5)$$

where p is the pressure of the perfect fluid.

The energy-momentum tensor of the system is conserved ($\nabla_\mu T^{\mu\nu} = 0$), however, both contributions are not conserved separately due to extra coupling term parametrized by the effective coupling of the fluid and scalar,

$$\nabla_\mu T_{\text{field}}^{\mu\nu} = -\nabla_\mu T_{\text{fluid}}^{\mu\nu} = \frac{\partial V}{\partial\phi}\partial^\nu\phi + \eta u^\mu\partial_\mu\phi\partial^\nu\phi, \quad (6)$$

where η is a constant parametrizing strength of this interaction [26].

We use spherical coordinates in space as they capture the symmetry of a single growing bubble that we intend to simulate. The final form of equations of motion and their discretization is described in the Supplemental Material [30].

The key parameters characterizing the transition are the nucleation temperature T_n at which at least one bubble appears per horizon and the amount of the vacuum energy released in the transition normalized to the energy of the radiation bath ρ_r . In the fluid approximation, it can be defined as

$$\alpha = \frac{\theta_s - \theta_b}{\rho_r} \Big|_{T=T_n}, \quad (7)$$

where θ is the trace anomaly in the symmetric (s) and broken (b) phase, given by the expression,

$$\theta = \frac{1}{4}(\epsilon - 3p). \quad (8)$$

Note, that this definition of the trace anomaly applied to the equation of state (1) and (2) corresponds to the standard definition of $\alpha = \frac{1}{\rho_r}(\Delta V - \frac{T}{4}\Delta\frac{\partial V}{\partial T})$ [54,55].

III. ANALYTICAL APPROXIMATION: BAG MODEL

A simple model describing analytically many important features of the late-time evolution of our system is the bag model [19]. It neglects the scalar field approximating its profile as a step function connecting the two vacua. The equation of state reads

$$\epsilon_s = 3a_s T_s^4 + \theta_s, \quad \epsilon_b = 3a_b T_b^4 + \theta_b, \quad (9)$$

$$p_s = a_s T_s^4 - \theta_s, \quad p_b = a_b T_b^4 - \theta_b, \quad (10)$$

where θ_s and θ_b correspond to the symmetric phase outside the bubble and broken phase inside, respectively. Assuming that the vacuum energy vanishes in the broken phase as the field is in the global minimum of the potential we have $\theta_b = 0$.

Therefore, the strength of the transition can be consistently defined with the Eq. (7). Assuming that the plasma is locally in equilibrium, the energy-momentum tensor can be parametrized for the perfect fluid as in Eq. (5). Conservation of $T_{\text{fluid}}^{\mu\nu}$ along the flow and its projection perpendicular to the flow, respectively, give

$$\partial_\mu(u^\mu w) - u_\mu\partial^\mu p = 0, \quad (11)$$

$$\bar{u}^\nu u^\mu w \partial_\mu u_\nu - \bar{u}^\nu \partial_\mu p = 0, \quad (12)$$

with $\bar{u}_\mu u^\mu = 0$ and $\bar{u}^2 = -1$. As there is no characteristic distance scale in the problem, the solution should depend only on the self-similar variable $\xi = r/t$, where r denotes the distance from the center of the bubble and t is the time since nucleation. Changing the variables, Eqs. (11) and (12) take the form

$$(\xi - v) \frac{\partial_\xi \epsilon}{w} = 2 \frac{v}{\xi} + [1 - \gamma^2 v(\xi - v)] \partial_\xi v, \quad (13)$$

$$(1 - v\xi) \frac{\partial_\xi p}{w} = \gamma^2 (\xi - v) \partial_\xi v, \quad (14)$$

and using the definition of the speed of sound in the plasma $c_s^2 \equiv \frac{dp}{dT} / \frac{d\epsilon}{dT}$ can be combined into the single equation describing the plasma velocity profile $v(\xi)$ in the frame of the bubble center

$$2 \frac{v}{\xi} = \gamma^2 (1 - v\xi) \left[\frac{\mu^2}{c_s^2} - 1 \right] \partial_\xi v, \quad (15)$$

with $\mu = \frac{\xi - v}{1 - \xi v}$ denoting the Lorentz-transformed fluid velocity. Solutions of Eq. (15) in general depend only on the transition strength α and bubble wall velocity in the stationary state ξ_w . In a similar way, analytical profiles for the enthalpy w , temperature T and other thermodynamical quantities can be obtained. Later we will refer to them to compare the results of our simulations with the analytical solutions. Detailed derivations are described in [15,19,56,57]. In general, there exist three types of the bubble wall profiles:

- (1) *Deflagrations* are the solutions with subsonic bubble wall velocity ξ_w . In such a case, the expanding bubble pushes the plasma in front of it, while behind the bubble wall plasma remains at rest. Typically, the value of v decreases with ξ in the range $[\xi_w, c_s]$ and vanishes for $\xi > c_s$. Therefore, a shock front at $\xi = c_s$ may appear if the transition is strong enough.
- (2) *Detonations* are supersonic solutions, for which bubble wall velocity exceeds the Jouget velocity c_J [see Eq. (16)]. In this type of profile, the wall hits plasma which remains at rest in front of the bubble. As fluid enters the broken phase, it is accelerated with its velocity decreasing smoothly and reaching zero at $\xi = c_s$.
- (3) *Hybrids* are combinations of the two types mentioned above. They are realized for $\xi_w \in [c_s, c_J]$ and possess features of deflagrations (shock front in front of the wall) and detonations (nonzero plasma velocity behind the wall known as a rarefaction wave).

The Jouget velocity c_J at which the shell around the bubble disappears and the solution shifts from hybrid to detonation is given by Chapman-Jouguet condition [15,58]

$$c_J = \frac{1}{\sqrt{3}} \frac{1 + \sqrt{3\alpha^2 + 2\alpha}}{1 + \alpha}. \quad (16)$$

This is a crucial threshold as in particle physics models the friction typically grows with the temperature. Thus, if for a given potential the strength is large enough for the wall to accelerate above this velocity, the disappearance of the heated fluid shell around the bubble also lowers the friction substantially. As a result, in simple extensions of the Standard Model, one does not expect to find detonations with wall velocity significantly below the speed of light. While such very fast walls are optimal for a strong GW signal they do not generate a significant baryon asymmetry. In fact, it is the velocity just below c_J that prove to produce the largest baryon yield due to increased temperature in the plasma surrounding the bubble [14–17]. However, for the purpose of our scans, the nonequilibrium part of the friction is a free parameter and we adjust it to obtain all stable solutions including detonations.

IV. RESULTS FROM NUMERICAL SIMULATIONS

In this section, we will discuss the results of our numerical simulations. Every simulation is performed on the lattice with spacing $\delta r = 0.01 \text{ GeV}^{-1}$ and time step $\delta t = 0.001 \text{ GeV}^{-1}$. The time duration of the evolution is large enough to asymptotically achieve stationary states and is set to $t_{\text{max}} = 120 \text{ GeV}^{-1}$. Similarly, the physical size of the lattice is fixed as $R = ct_{\text{max}}$ which is large enough to prevent reaching the boundaries by the bubbles, since they expand subluminally.

We initialize each simulation with the recently nucleated bubble, fixing the field configuration to the critical profile and setting $T = T_n$ and $v = 0$ everywhere. The procedure for determining nucleation temperature T_n and the critical profile is described in Supplemental Material [30].

We have begun with the validation of our method on two benchmark points studied in the existing literature. We also compared our stationary states and those predicted by the bag model described in the previous section finding very good agreement. Results and details of both comparisons can be found in the Supplemental Material [30].

The exact relation between the wall velocity ξ_w and the friction parameter η is not unique and depends not only on the strength of the transition α , but also on other parameters defining the scalar potential. We start with the dependence of the results on the vacuum expectation value of the scalar field. We verified that the friction scales proportionally to the inverse of field value in the true vacuum. This fully determines the position of the gap in terms of friction parameter and to provide general results we will use the normalized value of the friction $v_0\eta$ already including this scaling.

Next, we move on to the much more interesting dependence of the results on the nucleation temperature T_n . We study a set of different potentials for which the transition strength α and the critical temperature T_c , at which the two minima in the potential are degenerate, are both fixed. The other parameters in the potential are chosen such that they predict a set of different nucleation temperatures. The value of the friction parameter depends on the field content of the model and as a result, we keep it as a free parameter. We logarithmically vary it in the range $\eta/T_c \in [0.01, 1]$, independently checking around 75 values for every scalar potential which is enough to map all the allowed classes of solutions in each case.

Relations between the friction η and wall velocity ξ_w in a range of T_n are shown the upper panels of Figs. 1 and 2 for $\alpha = 0.05$ and $\alpha = 0.1$, respectively.

There we can see that higher nucleation temperatures lead to a wider velocity gap, while for lower temperatures, almost the entire range of wall velocities can be covered. Note that nucleation temperatures very close to the critical temperature limit the bubble wall velocity for both deflagrations and hybrids so the speed of sound is never reached.

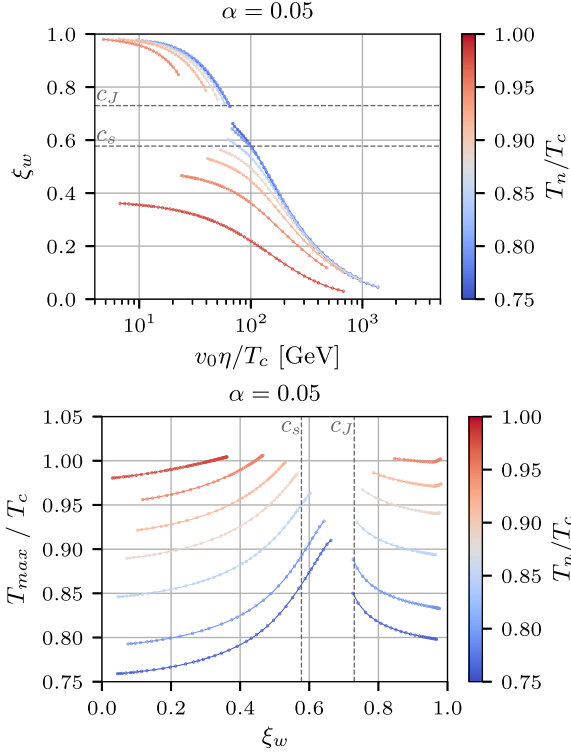


FIG. 1. Relation between the friction parameter η and bubble wall velocity in the stationary state ξ_w (upper panel) and the maximum of the plasma temperature along the profile (lower panel). Potentials are chosen such that the strength of the transition is fixed to $\alpha = 0.05$. The value of the nucleation temperature T_n is encoded with the color.

This dependence is made clearer in the lower panels of Figs. 1 and 2, where we show values of temperature at the peak of the bubble wall profile for different nucleation temperatures and values of α . As we see in general it is not possible to find a stationary state if the temperature in the profile significantly exceeds the critical temperature. This is an important condition for the part of the velocity gap below c_s and indeed this hydrodynamical obstruction was already proposed in the small velocity limit [20], where the authors derived an approximation for the maximal subsonic wall velocity. Our results agree roughly with this limit when the nucleation temperature is very close to the critical one. However, we found that a similar behavior continues for much lower temperatures and also supersonic solutions are affected. The mechanism itself in those cases becomes less straightforward as the instability sets in when the temperature reached within the shells is significantly below the critical one.

Our results show that a range of wall velocities is forbidden and the width of the gap depends on the relation between the critical and nucleation temperatures. The forbidden region is shown in Fig. 3 for the relatively large values of the transition strength which we studied. The upper limit showing the slowest possible detonations is

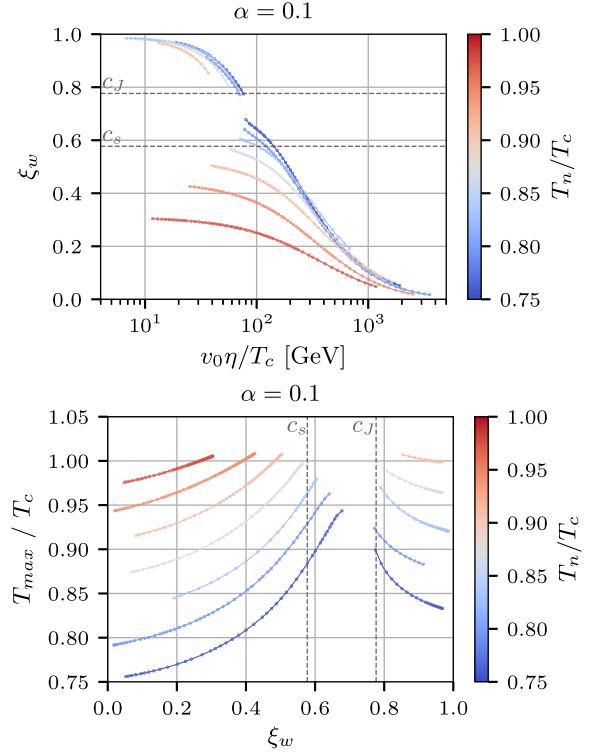


FIG. 2. Relation between the friction parameter η and bubble wall velocity in the stationary state ξ_w (upper panel) and the maximum of the plasma temperature along the profile (lower panel). Potentials are chosen such that the strength of the transition is fixed to $\alpha = 0.1$. The value of the nucleation temperature T_n is encoded with the color.

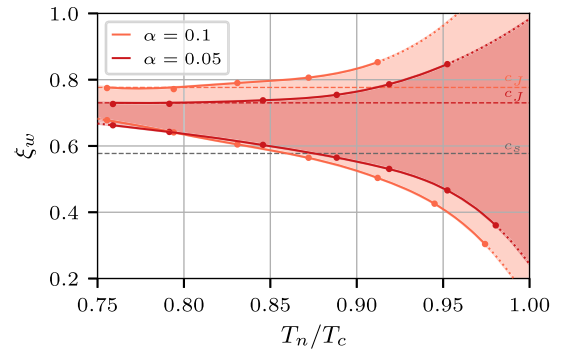


FIG. 3. Forbidden wall velocities (shaded regions) for two values of $\alpha = 0.1$ (orange) and $\alpha = 0.05$ (red). Dashed lines indicate the Jouguet velocities c_J [see Eq. (16)] and the speed of sound c_s . At high temperatures, hydrodynamic obstruction limits the velocities of both detonation and deflagration solutions. At lower temperatures detonations are realized above the Jouguet velocity as expected, however, we find the obstruction limiting the maximal velocity of hybrids persists resulting in a range of hydrodynamical solutions that are not realized. High-temperature part of the limit relies on extrapolation (dotted lines) and should be treated as a qualitative trend.

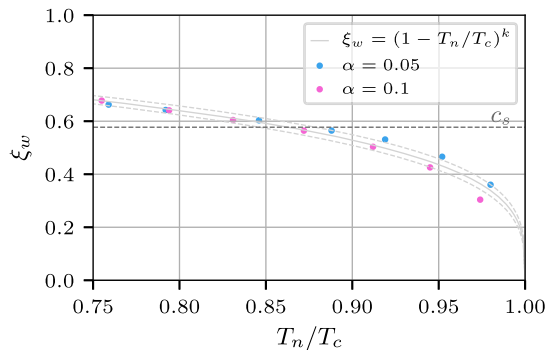


FIG. 4. The maximal wall velocity on the deflagration/hybrid branch computed in numerical simulations as a function of the nucleation temperature T_n together with the fit from Eq. (17) (solid line) and its variation within 3σ of the best-fit parameters (dashed lines).

explained through the Jouguet velocity at low temperatures and excessive heating when approaching the critical temperature. The lower limit corresponding to the fastest solutions predicting a heated fluid shell around the bubble is our main result. At high temperatures, it also corresponds to heating of the shell above the critical temperature yet it persists into supersonic solutions where the maximal temperature does not reach the critical one.

Figure 4 shows the maximal wall velocity reached by the deflagration/hybrid solutions as a function of the nucleation temperature for different transition strengths. Given that in limit of relatively large strength the result for hybrids does not depend significantly on α we found a simple fit

$$\xi_w^{\max} = \left(1 - \frac{T_n}{T_c}\right)^k \quad \text{with } k = 0.2768 \pm 0.0055, \quad (17)$$

also shown in the plot, which can be used as a rough approximation for the upper bound for wall velocities.

Direct verification of this mechanism in particle physics models is beyond the scope of this work, however, to assess its impact we checked our criterion against the points from scans of the Standard Model plus a neutral singlet presented in Ref. [17]. We found that nearly all wall velocities predicted there will be lowered as the walls cease to accelerate due to the obstruction before achieving the velocities predicted by the WKB approximation. We discuss the details of this comparison in the last section of the Supplemental Material [30].

V. SUMMARY

We investigate the fluid solutions realized in the presence of growing bubbles in cosmological first-order phase transitions. We use numerical lattice simulations using

spherical symmetry of the system and compare results to the well-known analytical solutions.

We found good agreement between the analytical profiles and our numerical results whenever the latter exist. Our key result, however, is that the hydrodynamical obstruction preventing the realization of fast hybrids is very generic. In fact, we always find some solutions to be forbidden and the gap in solutions becomes wider as the temperature at which bubbles nucleate predicted by the potential is closer to the critical temperature at which the minima in the potential are degenerate. In extreme cases where the temperatures are very close, no hybrid solutions are realized and as the friction drops the allowed solutions jump from subsonic deflagrations straight to detonations. The mechanism behind the obstruction is well understood in the case of deflagrations where the temperature profiles in the gap that are not realized would simply heat the plasma above the critical temperature and reverse the transition. In the case of hybrids the mechanism is more complicated and even solutions that do not reheat to such dangerous levels are not realized.

While the effect is yet to be confirmed directly in particular models we expect it to be general. Our calculations were performed for a simple toy potential, however, we express them in terms of general characteristics shared by all models predicting a first-order transition.

The existence of the velocity gap will have a crucial impact on predictions of models realizing electroweak baryogenesis. This is due to the fact that the fastest walls that did not accelerate enough to become detonations are the ones most likely to be affected and the effect would persist even in low temperatures. Such solutions were recently shown to predict the largest baryon yields. Thus our results are likely to exclude parts of the parameter space of models most promising for electroweak baryogenesis and impact their viability as solutions to the problem of baryon asymmetry.

ACKNOWLEDGMENTS

The authors would like to thank José Miguel No for fruitful discussions. This work was supported by the Polish National Agency for Academic Exchange within Polish Returns Programme under Agreement No. PPN/PPO/2020/1/00013/U/00001 and the Polish National Science Centre Grant No. 2018/31/D/ST2/02048. T. K. was supported by Grant No. 2019/32/C/ST2/00248 from the Polish National Science Centre. During the completion of this work, T. K. was supported by Grant No. 2019/33/B/ST9/01564 from the Polish National Science Centre. T. K. acknowledges the hospitality of Rudolf Peierls Centre for Theoretical Physics at Oxford University, where parts of this work have been done.

- [1] V. A. Kuzmin, V. A. Rubakov, and M. E. Shaposhnikov, *Phys. Lett.* **155B**, 36 (1985).
- [2] A. G. Cohen, D. B. Kaplan, and A. E. Nelson, *Annu. Rev. Nucl. Part. Sci.* **43**, 27 (1993).
- [3] V. A. Rubakov and M. E. Shaposhnikov, *Usp. Fiz. Nauk* **166**, 493 (1996).
- [4] D. E. Morrissey and M. J. Ramsey-Musolf, *New J. Phys.* **14**, 125003 (2012).
- [5] C. Caprini *et al.*, *J. Cosmol. Astropart. Phys.* 04 (2016) 001.
- [6] C. Caprini *et al.*, *J. Cosmol. Astropart. Phys.* 03 (2020) 024.
- [7] Y. A. El-Neaj *et al.* (AEDGE Collaboration), *Eur. Phys. J. Quantum Technol.* **7**, 6 (2020).
- [8] L. Badurina, O. Buchmueller, J. Ellis, M. Lewicki, C. McCabe, and V. Vaskonen, *Phil. Trans. R. Soc. A* **380**, 20210060 (2021).
- [9] J. M. Cline and K. Kainulainen, *Phys. Rev. D* **101**, 063525 (2020).
- [10] B. Laurent and J. M. Cline, *Phys. Rev. D* **102**, 063516 (2020).
- [11] G. C. Dorsch, S. J. Huber, and T. Konstandin, *J. Cosmol. Astropart. Phys.* 08 (2021) 020.
- [12] G. C. Dorsch, S. J. Huber, and T. Konstandin, *J. Cosmol. Astropart. Phys.* 04 (2022) 010.
- [13] J. M. Cline, A. Friedlander, D.-M. He, K. Kainulainen, B. Laurent, and D. Tucker-Smith, *Phys. Rev. D* **103**, 123529 (2021).
- [14] J. M. Cline and B. Laurent, *Phys. Rev. D* **104**, 083507 (2021).
- [15] M. Lewicki, M. Merchand, and M. Zych, *J. High Energy Phys.* 02 (2022) 017.
- [16] B. Laurent and J. M. Cline, *Phys. Rev. D* **106**, 023501 (2022).
- [17] J. Ellis, M. Lewicki, M. Merchand, J. M. No, and M. Zych, *J. High Energy Phys.* 01 (2023) 093.
- [18] J. M. No, *Phys. Rev. D* **84**, 124025 (2011).
- [19] J. R. Espinosa, T. Konstandin, J. M. No, and G. Servant, *J. Cosmol. Astropart. Phys.* 06 (2010) 028.
- [20] T. Konstandin and J. M. No, *J. Cosmol. Astropart. Phys.* 02 (2011) 008.
- [21] J. Ignatius, K. Kajantie, H. Kurki-Suonio, and M. Laine, *Phys. Rev. D* **49**, 3854 (1994).
- [22] H. Kurki-Suonio and M. Laine, *Phys. Rev. D* **54**, 7163 (1996).
- [23] H. Kurki-Suonio, K. Jedamzik, and G. J. Mathews, *Astrophys. J.* **479**, 31 (1997).
- [24] M. Hindmarsh, S. J. Huber, K. Rummukainen, and D. J. Weir, *Phys. Rev. Lett.* **112**, 041301 (2014).
- [25] M. Hindmarsh, S. J. Huber, K. Rummukainen, and D. J. Weir, *Phys. Rev. D* **92**, 123009 (2015).
- [26] Assuming local thermal equilibrium and neglecting the fluid-plasma coupling η one can obtain analytical results [27–29] for the wall velocity.
- [27] S. Balaji, M. Spannowsky, and C. Tamarit, *J. Cosmol. Astropart. Phys.* 03 (2021) 051.
- [28] W.-Y. Ai, B. Garbrecht, and C. Tamarit, *J. Cosmol. Astropart. Phys.* 03 (2022) 015.
- [29] W.-Y. Ai, B. Laurent, and J. van de Vis, *J. Cosmol. Astropart. Phys.* 07 (2023) 002.
- [30] See Supplemental Material at <http://link.aps.org/supplemental/10.1103/PhysRevD.108.103523> for details on the equations of motion and their numerical realization as well as validation on benchmarks discussed in the existing literature. There we also compare our results with existing literature on the wall velocity predicted in the Standard Model supplemented with a neutral singlet. The Supplemental Material includes Refs. [31–53].
- [31] M. Kamionkowski and K. Freese, *Phys. Rev. Lett.* **69**, 2743 (1992).
- [32] W. Tang and Y. Sun, *Appl. Math. Comput.* **219**, 2158 (2012).
- [33] E. Gagarina, V. Ambati, J. van der Vegt, and O. Bokhove, *J. Comput. Phys.* **275**, 459 (2014).
- [34] S. Zhao and G. W. Wei, *Math. Models Methods Appl. Sci.* **37**, 1042 (2014).
- [35] C. M. Campos, High order variational integrators: A polynomial approach, in *Advances in Differential Equations and Applications*, edited by F. Casas and V. Martínez (Springer International Publishing, Cham, 2014), pp. 249–258.
- [36] S. Ober-Blöbaum and N. Saake, arXiv:1304.1398.
- [37] E. Gagarina, V. Ambati, S. Nurijanyan, J. van der Vegt, and O. Bokhove, *J. Comput. Phys.* **306**, 370 (2016).
- [38] M. Muehlebach, T. Heimsch, and C. Glocker, *Int. J. Numer. Methods Eng.* **109**, 1549 (2016).
- [39] S. Ober-Blöbaum, IMA J. Numer. Anal. **37**, 375 (2016).
- [40] D. Kuzmin and S. Turek, *J. Comput. Phys.* **175**, 525 (2002).
- [41] D. Kuzmin, M. Möller, and S. Turek, *Int. J. Numer. Methods Fluids* **42**, 265 (2003).
- [42] M. Möller, *Computing* **95**, 425 (2013).
- [43] D. Kuzmin, *Comput. Methods Appl. Mech. Eng.* **373**, 113569 (2021).
- [44] S. T. Zalesak, *J. Comput. Phys.* **31**, 335 (1979).
- [45] S. T. Zalesak, The design of flux-corrected transport (FCT) algorithms for structured grids, in *Flux-Corrected Transport: Principles, Algorithms, and Applications*, edited by D. Kuzmin, R. Löhner, and S. Turek (Springer Netherlands, Dordrecht, 2012), pp. 23–65, 10.1007/978-94-007-4038-9_2.
- [46] E. Kunhardt and C. Wu, *J. Comput. Phys.* **68**, 127 (1987).
- [47] M. Lewicki, V. Vaskonen, and H. Veermäe, *Phys. Rev. D* **106**, 103501 (2022).
- [48] S. R. Coleman, *Phys. Rev. D* **15**, 2929 (1977); **16**, 1248(E) (1977).
- [49] C. G. Callan, Jr. and S. R. Coleman, *Phys. Rev. D* **16**, 1762 (1977).
- [50] A. D. Linde, *Phys. Lett.* **100B**, 37 (1981).
- [51] A. D. Linde, *Nucl. Phys.* **B216**, 421 (1983); **B223**, 544(E) (1983).
- [52] J. Ellis, M. Lewicki, and J. M. No, *J. Cosmol. Astropart. Phys.* 04 (2019) 003.
- [53] F. C. Adams, *Phys. Rev. D* **48**, 2800 (1993).
- [54] M. Hindmarsh, S. J. Huber, K. Rummukainen, and D. J. Weir, *Phys. Rev. D* **96**, 103520 (2017); **101**, 089902(E) (2020).
- [55] P. Auclair *et al.* (LISA Cosmology Working Group), *Living Rev. Relativity* **26**, 5 (2023).
- [56] M. Hindmarsh and M. Hijazi, *J. Cosmol. Astropart. Phys.* 12 (2019) 062.
- [57] J. Ellis, M. Lewicki, and J. M. No, *J. Cosmol. Astropart. Phys.* 07 (2020) 050.
- [58] P. J. Steinhardt, *Phys. Rev. D* **25**, 2074 (1982).